NANO LETTERS

pubs.acs.org/NanoLett

Letter

Nanoscale-Resolved Surface-to-Bulk Electron Transport in $CsPbBr_3$ Perovskite

Serhii Polishchuk, Michele Puppin, Alberto Crepaldi, Gianmarco Gatti, Dmitry N. Dirin, Olga Nazarenko, Nicola Colonna, Nicola Marzari, Maksym V. Kovalenko, Marco Grioni, and Majed Chergui*

Cite This: *Nano Lett.* 2022, 22, 1067−1074

Read Online

ACCESS | Metrics & More | Article Recommendations | Supporting Information

ABSTRACT: Describing the nanoscale charge carrier transport at surfaces and interfaces is fundamental for designing high-performance optoelectronic devices. To achieve this, we employ time- and angle-resolved photoelectron spectroscopy with ultraviolet pump and extreme ultraviolet probe pulses. The resulting high surface sensitivity reveals an ultrafast carrier population decay associated with surface-to-bulk transport, which was tracked with a sub-nanometer spatial resolution normal to the surface, and on a femtosecond time scale, in the case of the inorganic $CsPbBr_3$ lead halide perovskite. The decay time exhibits a pronounced carrier density dependence, which is attributed via modeling to enhanced diffusive transport and concurrent recombination. The transport is found to approach an ordinary diffusive regime, limited by electron−hole scattering, at the highest excitation fluences. This approach constitutes an important milestone in our capability to probe hot-carrier transport at solid interfaces with sub-nanometer resolution in a theoretically and experimentally challenging, yet technologically relevant, high-carrier-density regime.

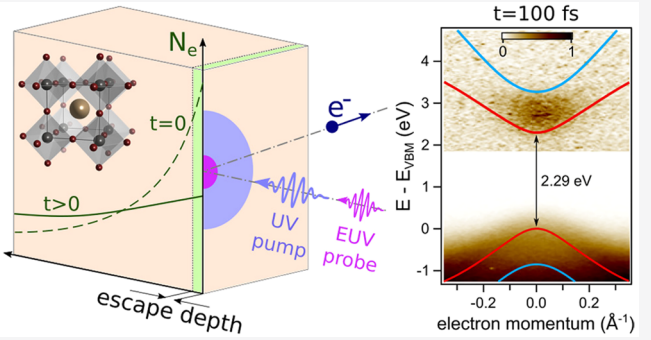

KEYWORDS: *nanoscale charge carrier transport, diffusion, ultrafast photoelectron spectroscopy, electronic structure, semiconductors, lead halide perovskites*

A profound understanding and a reliable description of charge carrier transport at the nanometer length scale are crucial for a multitude of optoelectronic applications. In bulk materials with large absorption coefficients, such as lead halide perovskites (LHPs),[1] strong gradients of carrier density occur on the nanometer scale and transport phenomena are expected to take place in a femtosecond regime. These surface or interface transport processes are central for the operation of single-junction and tandem solar cells,[2−4] nanolasers,[5−7] light-emitting diodes (LEDs),[8] and photocatalytic systems.[9,10] From a spatial perspective, while recent advances in ultrafast optical imaging have made outstanding contributions in characterizing the lateral transport of charge carriers,[11−14] these studies lack the ability to monitor the surface-to-bulk transport, which as a consequence has remained elusive up to now.[15] In addition, these techniques do not have a sensitivity to the electron momentum, which is crucial in discerning properties of band gap edge carriers.[16−18] From a temporal perspective, the hundreds of femtoseconds time scales are intricate due to a crossover between the ballistic[12] and the diffusive[11,13,14,19] transport regimes, making either analytical or numerical description difficult. In this work, we overcome these limitations by monitoring the ultrafast dynamics of photo-excited electrons using time- and angle-resolved photoelectron spectroscopy (TR-ARPES),[16,20,21] supported by theoretical modeling. We apply this approach to the case of the inorganic lead halide perovskite $CsPbBr_3$ upon ultraviolet (UV) excitation, creating a strong charge gradient at the surface. Vital to this strategy is the use of extreme ultraviolet (EUV) probe pulses. Indeed, in solids containing heavy elements (such as Pb and Br), the inelastic mean free path (MFP) of photoelectrons at 20−30 eV photon energies is ∼5 Å.[22] Unlike the case of bulk-integrating techniques, this extreme surface sensitivity is used to extract information about the carrier transport on a sub-nanometer scale in the direction orthogonal to the surface (along the *z* axis in Figure 1). This unique capability, combined with femtosecond temporal and momentum resolution, enables us to selectively follow in real space

Received: October 26, 2021
Revised: January 2, 2022
Published: January 19, 2022

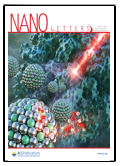

https://doi.org/10.1021/acs.nanolett.1c03941
Nano Lett. 2022, 22, 1067−1074

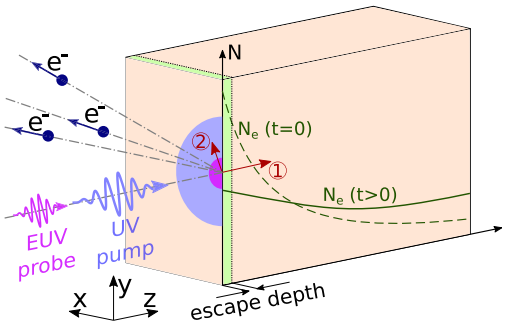

Figure 1. Schematic view of the experiment. The numbered arrows correspond to (1) carrier transport into the bulk and (2) lateral transport across the surface.

and real time the ultrafast evolution of the electron population in the conduction band (CB).

LHPs earned their place among the most studied semiconductors due to their outstanding optoelectronic properties,[23,24] which can be engineered by small modifications in composition and structure,[25,26] adapting them for a wide variety of applications.[27−29] LHPs possess some remarkable transport properties, such as long carrier lifetimes,[30−32] carrier effective mass renormalization,[17,33,34] and defect tolerance,[35,36] which were partially attributed to polaron formation. The complexity in describing carrier transport in LHPs is due to a delicate interplay of electronic and lattice dynamics with disorder and defects.[37−41] Furthermore, their transport properties can be strongly influenced by the operating conditions of a photonic device.[42,43] Many applications, such as LEDs, lasers, and solar concentrators,[44] typically operate under high carrier densities, where, in view of an enhanced long-term stability,[45−47] fully inorganic LHPs are better suited in comparison to their hybrid counterparts. At charge carrier densities above ~10^{18} cm^{-3}, complex many-body phenomena can be observed in LHPs,[48−50] such as hot-phonon bottleneck[51−54] and band-filling[55] effects, Auger processes become an important recombination channel for photocarriers,[56,57] an excitonic Mott transition occurs,[5] and the polaronic transport picture breaks down.[48] Photophysical studies of LHPs in this convoluted yet technologically relevant regime are theoretically and experimentally challenging.[58−63]

Here, we monitor the charge carrier dynamics of $CsPbBr_3$ single crystals by TR-ARPES as a function of carrier density. The observed evolution of the photoemission signal reflects the migration of near-surface carriers into the bulk on a time scale that depends significantly on the carrier density. With the support of modeling based on diffusion and recombination rate equations, our study of strongly photoexcited samples (~10^{19}−10^{20} cm^{-3}) reveals that at lower densities the carrier diffusivity is strongly enhanced, possibly due to high velocities of hot carriers, sustained by band-filling, hot-phonon bottleneck, and Auger heating[56] effects, resulting in a fast decay of surface population. However, at higher densities, the transport is predominantly limited by carrier−carrier scattering and can be described by conventional diffusivity already at ultrafast time scales.

The experimental scheme is depicted in Figure 1. The UV pump pulse initially creates a depth distribution of photocarriers with an exponentially decaying profile inside the crystal (dashed line). The EUV probe pulse then photoemits primary electrons from a small volume, indicated in green. A change in the carrier density (solid line) in the probed volume is reflected in the photoemission signal strength, which provides a direct access to the evolution of the carrier population.

Figure 2a shows the ARPES intensity plotted as a function of the k_x and k_y in-plane components of the electron momentum,

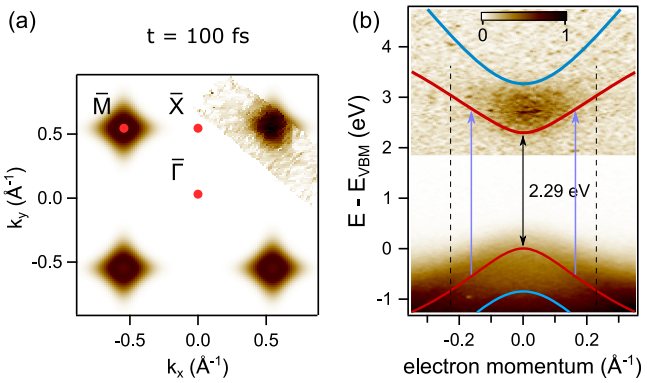

Figure 2. Electronic structure of $CsPbBr_3$: (a) experimentally measured constant energy map as a function of the in-plane electron momentum of the lowest CB (shown in the top right corner) overlapped with a DFT simulation; (b) Dispersions of the VB and the CB measured at t = 100 fs (the color scale of the upper part of the image was multiplied by a factor of 5) overlapped with the DFT bands at $k_z = \pi/a$ (red) and $k_z = 0$ (blue). Black dashed lines indicate the integration range used to obtain Figure 3. Violet arrows indicate the allowed pump excitation. Note: the experimental surface sensitivity leads to an additional partial integration along the k_z, as explained in ref 17.

acquired at 2.6 eV above the valence band (VB) maximum immediately after (t = 100 fs) the pump excitation. The measured constant energy map is overlapped with density functional theory (DFT) calculations and shows localized electron pockets at the corners ($\bar{M}$ point) of the surface Brillouin zone (SBZ) corresponding to the (001) lattice plane.[17] When the probe energy is tuned, the maximum CB intensity is observed at 24.3 eV, close to the R point of the three-dimensional BZ.[64] In what follows we exploit the energy tunability and the momentum resolution of ARPES to observe the electron dynamics at the CB minimum.

Figure 2b shows the dispersion of the bands forming the band gap, measured using 24.3 eV probe energy, at t = 100 fs after the excitation (indicated by violet arrows). For the first time, the energy-momentum dispersions of both the occupied and the unoccupied states are resolved simultaneously. Red and blue solid lines depict the theoretical dispersion of band gap edges as a function of the electron momentum orthogonal to the surface for the two extreme values $k_z = \pi/a$ and $k_z = 0$, respectively. The band gap magnitude was matched to the value determined via optical absorption (~2.29 eV, section 2.3 in the Supporting Information). It agrees with other optical data from the literature (2.2−2.4 eV)[1,65,66] and with combined direct and inverse photoemission studies (2.3 eV).[25,67] This ensures that the experiment probes the electron dynamics at the minimum of the CB.

Experimental (for the VB) and theoretical investigations indicate that the states forming the band gap of $CsPbBr_3$ have a nearly parabolic dispersion isotropic in all three directions of the momentum space.[16−18,68] Possible direct electronic transitions for the 3.2 eV pump energy are indicated by violet arrows in Figure 2b. The maximum photocarrier excess energy

https://doi.org/10.1021/acs.nanolett.1c03941
Nano Lett. 2022, 22, 1067−1074

of ~0.9 eV is insufficient to promote electrons to higher energy valleys (see Figure S3). Therefore, the electron population is restricted exclusively to the lowest energy valley of the BZ.

Figure 3a shows photoemission intensity maps integrated in the momentum range of ±0.23 Å^{-1} around the $\bar{M}$ point

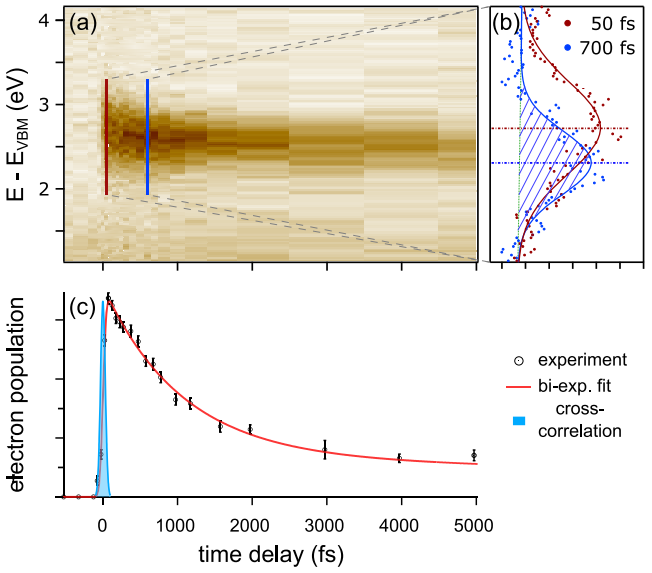

Figure 3. TR-ARPES data: (a) time evolution of the integrated photoemission intensity maps (the integration range is indicated by dashed lines in Figure 2b); (b) Gaussian fits of the integrated maps at the two time delays indicated by vertical lines in (a); (c) temporal dynamics of the CB population with a biexponential fit to the data. The time delay of 0 fs is fixed at the half-rise of the signal. The error bars indicate standard deviations of the Gaussian fit of the peak areas. The blue Gaussian represents the cross-correlation of the pump and probe pulses.

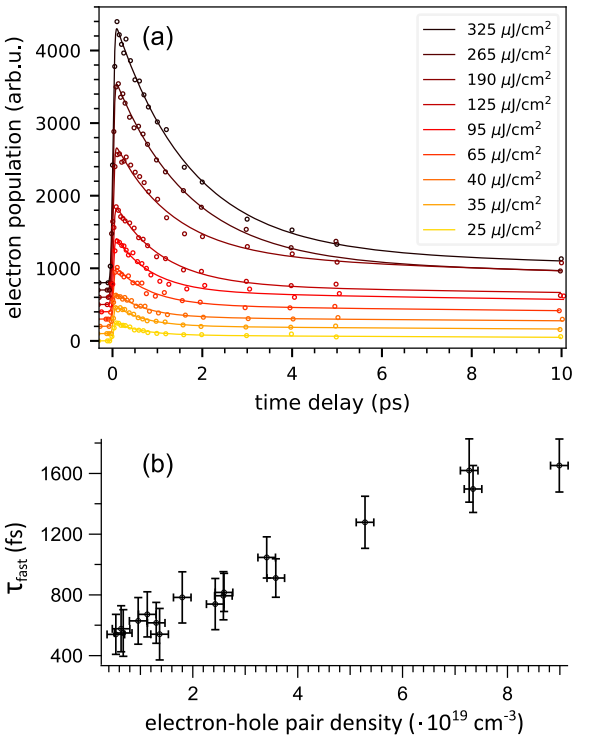

Figure 4. Temporal evolution of the CB population (a) Biexponential fits (lines) to the experimental data (circles). The legend shows the incident pump fluence of the corresponding scan. The traces are offset by 100 arb.u. for better visibility. (b) The time scale of the fast decay component τ_{fast} as a function of electron−hole pair density in the probed volume. The vertical error bars indicate standard deviations of the plotted fit parameters. The horizontal error bars indicate estimated uncertainties originating from pump power fluctuations.

(between black dashed lines in Figure 2b), plotted vs time delay, and shows the evolution of the CB population. The integrated maps were fitted with a Gaussian, as shown in Figure 3b. The peak area is proportional to the photoexcited electron population and is shown in Figure 3c, as a function of time delay. The CB population increases upon UV excitation within our temporal resolution (~70 fs), and it decays on a picosecond time scale.

The decay is well fitted with a double-exponential function, pointing to at least two underlying processes. To elucidate the role of the carrier density on the CB dynamics, we investigated the dependence of the extracted decay time constants as a function of the incident pump fluence in the range of (25−325) ± 5 μJ/cm^2. The experimental traces and the corresponding fits are shown in Figure 4a. The maximum electron population scales linearly with the excitation fluence, indicating that the experiments are conducted within a linear absorption regime (section 2.7 in the Supporting Information). Furthermore, a progressively slower population decay at higher fluences is visually apparent.

The time constant of the fast-decay component is denoted as τ_{fast} and that of the slower contribution as τ_{slow}. The fast time scale τ_{fast} is weakly affected by the choice of τ_{slow} for all of the pump fluences (section 2.9 in the Supporting Information), and a good agreement with the experimental traces is retained when they are fitted globally with a single τ_{slow}, yielding a value of ~20 ps.

The increase of τ_{fast} as a function of photogenerated electron−hole pair density N in the probed volume (section 2.6 in the Supporting Information) is shown in Figure 4b. It increases 3-fold over the entire range of probed densities.

Taking into account the extreme surface sensitivity and the picosecond time scale of the population decay, we consider carrier recombination within and transport out of the probed volume (indicated as (1) in Figure 1) to be the most likely pathways. In particular, our analysis, detailed below, reveals that in the high-N regime the carrier transport is limited by electron−hole scattering and can be accounted for by steady-state diffusion with a strong contribution of Auger recombination (AR). However, at low N, we observe a fast transport characterized by anomalously high values of diffusivity, reflecting a significant contribution from carriers that have undergone few or no scattering events (quasi-ballistic transport).

In order to provide a quantitative insight into the transport and recombination properties of $CsPbBr_3$, we modeled them numerically, considering the carrier diffusion and the trap-assisted surface recombination, along with various electron−hole recombination pathways within the bulk, as being potentially responsible for the population dynamics in the probed volume. Subsequently, we model the depth−temporal profile $N(z,t)$ of the carrier density inside the crystal to compare it with the near-surface density evolution tracked experimentally. We proceed by solving the differential equation

https://doi.org/10.1021/acs.nanolett.1c03941
Nano Lett. 2022, 22, 1067−1074

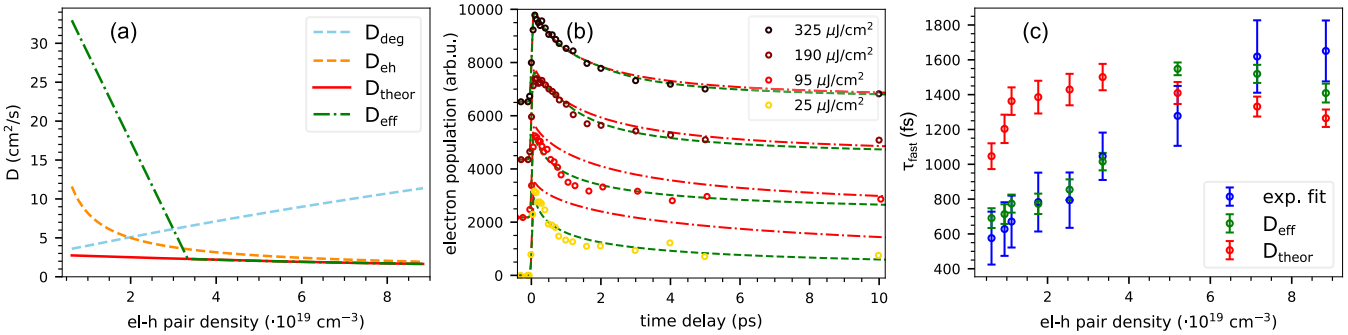

Figure 5. Results of modeling charge carrier density evolution in the probed volume: (a) carrier density dependence of the diffusion coefficient originating from carrier degeneracy (D_{deg}, blue) and electron−hole scattering (D_{eh}, orange), overlapped with the combined dependence calculated according to Matthiessen's rule (D_{theor}, red) and with the effective diffusivity extracted from the global fit of the solutions of eq 1 to the experimental data under the assumption of its linear variation at low N (D_{eff}, green); (b) comparison of selected simulated traces (with normalized amplitude) extracted by solving eq 1, incorporating the diffusivity dependences $D(N)$ depicted in (a) by red and green, correspondingly; (c) comparison of density dependences of τ_{fast} extracted from global biexponential fits to the experimental data (blue) and to the green and red traces in (b), correspondingly. The error bars indicate standard deviations of the plotted fit parameters.

$$\frac{\partial N(z,t)}{\partial t} = D\frac{\partial^2 N}{\partial z^2} - k_1 N - k_2 N^2 - k_3 N^3 + G(z,t)$$
$$\frac{\partial N(z,t)}{\partial z}\Big|_{z=0} = \frac{S}{D}N(0,t), \quad N(\infty,t) = 0$$
$$N(z,-\infty) = 0 \tag{1}$$

which is often adopted in photoemission[69,70] and optical studies.[71−74] Here, D is the diffusion coefficient, S is the surface recombination velocity,[45] and k_1, k_2, and k_3 are the mono-,[66] bi-, and trimolecular (AR) bulk recombination coefficients,[71,75,76] respectively. The term $G(z,t)$ represents carrier generation and follows the temporal and spatial profiles of the pump. Various other processes, including a photo-Dember effect,[77] surface photovoltage, and lateral transport (indicated as (2) in Figure 1), act on longer time scales (section 2.11 in the Supporting Information) and therefore are not included in the model.

At photocarrier densities above the onset of many-body effects in LHPs, the density dependence of the bimolecular $k_2(N)$, the AR $k_3(N)$, and the diffusion $D(N)$ coefficients[71,72] must be considered. The last coefficient stems from numerous mechanisms, such as the saturation of trap states at low densities or the increased effect of carrier degeneracy and of electron−hole scattering at high densities.[13,71,72] The diffusivity D is expected to increase with N due to degeneracy according to the generalized Einstein relation.[72] The resulting dependence, calculated using optical data from ref 71, is shown by the blue line in Figure 5a. Concurrently, a more efficient electron−hole scattering at higher N results in an asymptotic $\sim 1/N$ dependence,[13] shown by the orange line in Figure 5a, which was calculated using reported values of the static permittivity[78] and of the reduced carrier effective mass.[79] The value combined via Matthiessen's rule, as $1/D_{theor}(N) = 1/D_{deg}(N) + 1/D_{eh}(N)$, is plotted as the red line in Figure 5a.

The bi- and trimolecular recombination coefficients are expected to reduce and saturate at high carrier densities due to an increased Coulomb screening[80] and state filling.[72] The corresponding approximation for $k_2(N)$ was adopted from ref 71. To model the saturation of $k_3(N)$, we used the heuristic form $k_3 = k_{30}/(1 + N/N_g)^{3/2}$, proposed in the literature,[72] and the experimental values $k_{30} = 3.6 \times 10^{-27}$ cm^6 s^{-1} and $N_g = 7 \times 10^{18}$ cm^{-3}.[71,72] This implies a gradual decrease in k_3 by 1 order of magnitude within our range of N (section 2.12 in the Supporting Information). According to our band structure calculations, $CsPbBr_3$ possesses a so-called coincidental resonance between the band gap and an interband transition in the VB (unlike the CB) (section 2.2 in the Supporting Information), also reported for the CB of $MAPbI_3$.[81] Therefore, the hhe AR process (involving two holes and one electron) is expected to dominate over the eeh process. The latter is, nonetheless, possible in the form of phonon-assisted AR, which is usually dominant in degenerate wide-gap semiconductors.[80,82]

After incorporation of the density dependence of various coefficients into eq 1, the experiment was matched only at high carrier densities, as shown by the red traces in Figure 5b. Conversely, the model strongly underestimates the decay at lower carrier densities, as shown in Figure 5c, which compares the values of τ_{fast} extracted from the global fit to the experimental data (in blue) and to the simulated traces (in red) displayed in Figure 5b, pointing toward additional mechanisms at low densities. In fact, an accelerated non-equilibrium transport persisting for tens of picoseconds is expected to occur in LHPs when the photocarriers have sufficient excess energy, as demonstrated by a recent experimental study.[42] Under such conditions, the effective diffusivity can exceed the equilibrium value by 2 orders of magnitude. To quantify the possible deviation from the conventional transport model, we extract an effective diffusivity $D_{eff}(N)$ by globally minimizing the mismatch between the experiment and the simulation using a modified model, in which the diffusivity can vary under a certain N, assuming a linear dependence for simplicity. The resulting green traces in Figure 5b exhibit a significantly improved agreement with the experiment. This is also seen when the corresponding τ_{fast} values in Figure 5c (in green) are compared with the experimental values (in blue).

In a striking manner, Figure 5a shows that the extracted $D_{eff}(N)$ (green line) surpasses the equilibrium values (red line), which describe the steady-state transport,[71,72] by almost 1 order of magnitude at low densities. When the ultrashort time scale accessible by our experiments is considered, the enhanced transport of hot carriers can explain the fast population decay. In line with our findings, even higher

https://doi.org/10.1021/acs.nanolett.1c03941
Nano Lett. 2022, 22, 1067−1074

nonequilibrium diffusion coefficients (~100 cm^2/s), in comparison to ours (cm^2/s), were observed in the optical microscopy study of lateral transport on a picosecond time scale at a lower density (4×10^{-17} cm^{-3}) and at a higher excess energy (1.49 eV) of the photocarriers.[42]

Another similar study observed carriers in LHPs propagating ballistically over 150 nm within the first 20 fs upon light absorption.[12] Moreover, the transport length was found to be reduced with increasing N, due to enhanced carrier−carrier scattering, reaching a value of 66 ± 10 nm at $N = 0.25 \times 10^{19}$ cm^{-3}. This suggests that the ballistic transport lengths should be even shorter at our carrier densities.

According to diffusion theory, D is proportional to the photocarrier effective transport MFP λ_{eff} and to the average carrier velocity v: $D \approx v\lambda_{eff}$.[83,84] According to Matthiessen's rule, $1/\lambda_{eff} = \sum_i 1/\lambda_i$, where λ_i values are the individual MFPs related to the corresponding microscopic scattering mechanisms. In view of this, the shape of $D_{eff}(N)$ in Figure 5a can be qualitatively interpreted as follows: At low N, λ_{eff} is long and is limited by scattering with longitudinal optical (LO) phonons.[71] When λ_{eff} is comparable[84] to the probing depth, the electrons appear to leave the probed volume quasi-ballistically. This, together with the high velocities of hot carriers, leads to the observed enhanced diffusive transport. Three additional effects can contribute to the increased values of D: the hot-phonon bottleneck and Auger heating can maintain high carrier velocities by slowing down their cooling, whereas the polaron formation can increase λ_{eff} by screening the carrier electrostatic potential.[85]

The impact of carrier−carrier scattering increases at high N and results in λ_{eff} becoming shorter than the probing depth. This explains why the diffusivity in this regime agrees with studies of steady-state transport properties and asymptotically approaches the $1/N$ dependence. Ultimately, this reflects the dominance of carrier−carrier scattering as the main transport-limiting mechanism at high N. According to Figure 5c, this regime sets in above ~5×10^{19} cm^{-3}, where the conventional diffusion model starts to adequately describe the carrier transport at interfaces, even on a sub-picosecond time scale.

To summarize, the dominant mechanisms of carrier transport and recombination depend on a multitude of factors during the operation of an optoelectronic device, such as the surface contact (as in photocatalysis), the carrier density (as in solar cells vs solar concentrators), the time scale (as in pulsed lasers), and the length scale (as in nanoscale devices). In the case of $CsPbBr_3$, where the absorption depth is only ~60 nm, the carrier cooling, recombination, scattering, and transport develop a prominent depth dependence, following the photocarrier density distribution. A fundamental understanding of ultrafast processes driving carriers from interfaces toward the bulk (or e.g. the electrical contacts) is essential for improving device efficiencies. The tools capable of directly accessing these material properties are in great demand, as they are indispensable in developing qualitative and quantitative guidelines for mitigating functional bottlenecks and optimizing the performance. The EUV-based TR-ARPES provides a unique view of charge carrier dynamics, as it can selectively follow photocarriers at true band gap edges to extract the most precise and relevant photophysical characteristics. The ability to control the surface and bulk properties (such as doping, orientation, structure, etc.) of LHPs[25,27,28] and to choose the best operating conditions to take advantage of the density dependence of various many-body effects make LHPs an exciting material to be custom-tailored for next-generation applications: whether we want, for example, to enhance the radiative recombination, to maximize the transport length, or to minimize the carrier cooling rate, depending on the requirements. This approach is generally applicable to other technologically relevant semiconductors by selecting suitable pump and probe energies, whereas recent advances in nano-ARPES[86] expand its applicability even to nanosized samples. Future studies with energy-tunable excitation could further elucidate the role of carrier excess energy in the nanoscale transport.

From a theoretical perspective, our simulations highlight the limitations in applying the conventional diffusion theory to the nanoscale transport, prompting the community to further advance our capability of calculating nonequilibrium transport properties *ab initio*, upon unveiling their crucial role on the ultrafast time scale.

In conclusion, we utilized the surface sensitivity, temporal, and momentum resolution of EUV-based TR-ARPES to investigate the dynamics of electrons photoexcited into the conduction band of $CsPbBr_3$ single crystals. This allowed us to observe ultrafast electron transport into the bulk with sub-nanometer resolution, which we studied as a function of pump fluence. By combining our experimental results with simulations of the spatiotemporal evolution of the hot-electron population, we clarify the microscopic mechanisms governing the ultrafast surface-to-bulk carrier transport and recombination. This allows us to distinguish the carrier-density-dependent crossover from the enhanced to the ordinary diffusive transport regime at ~5×10^{19} cm^{-3}, with the former being limited by LO phonon scattering and the latter by carrier−carrier scattering. The results are consistent with the saturation of carrier recombination coefficients due to phase-space filling and Coulomb screening mechanisms enhanced at high carrier densities. Our results constitute a new milestone in understanding and describing the ultrafast nanoscale surface-to-bulk hot-carrier transport in LHPs in the high-carrier-density regime, which represents the operational conditions of various photonic and nano-optoelectronic devices. This approach can be generally implemented for studying nanoscale transport in all highly absorbing photonic materials, even beyond LHPs.

■ ASSOCIATED CONTENT

Supporting Information

The Supporting Information is available free of charge at https://pubs.acs.org/doi/10.1021/acs.nanolett.1c03941.

Materials and methods, estimation of TR-ARPES setup resolution, additional details of theoretical band structure calculations, absorption and photoluminescence spectra of the samples, details and discussion about surface band banding and space charge effects, estimation of the charge carrier density, linearity of pump absorption, estimation of the threshold density of polaron overlap, details of global fits to the data, estimate of the pump-induced surface temperature increase, discussion about the contribution of additional mechanisms to the conduction band intensity decay, and details about the numerical simulation of the electron population decay (PDF)

https://doi.org/10.1021/acs.nanolett.1c03941
Nano Lett. 2022, 22, 1067−1074

AUTHOR INFORMATION

Corresponding Author

Majed Chergui − *Laboratoire de Spectroscopie Ultrarapide (LSU) and Lausanne Centre for Ultrafast Science (LACUS), École Polytechnique Fédérale de Lausanne, ISIC, 1015 Lausanne, Switzerland;* orcid.org/0000-0002-4856-226X; Email: majed.chergui@epfl.ch

Authors

Serhii Polishchuk − *Laboratoire de Spectroscopie Ultrarapide (LSU) and Lausanne Centre for Ultrafast Science (LACUS), École Polytechnique Fédérale de Lausanne, ISIC, 1015 Lausanne, Switzerland;* orcid.org/0000-0001-5535-0479

Michele Puppin − *Laboratoire de Spectroscopie Ultrarapide (LSU) and Lausanne Centre for Ultrafast Science (LACUS), École Polytechnique Fédérale de Lausanne, ISIC, 1015 Lausanne, Switzerland;* orcid.org/0000-0002-1328-7165

Alberto Crepaldi − *Institute of Physics and Lausanne Centre for Ultrafast Science (LACUS), École Polytechnique Fédérale de Lausanne, 1015 Lausanne, Switzerland; Dipartimento di Fisica, Politecnico di Milano, Milan 20133, Italy*

Gianmarco Gatti − *Institute of Physics and Lausanne Centre for Ultrafast Science (LACUS), École Polytechnique Fédérale de Lausanne, 1015 Lausanne, Switzerland*

Dmitry N. Dirin − *Laboratory of Inorganic Chemistry, Department of Chemistry and Applied Biosciences, ETH Zürich, 8093 Zürich, Switzerland; Laboratory for Thin Films and Photovoltaics, EMPA−Swiss Federal Laboratories for Materials Science and Technology, 8600 Dübendorf, Switzerland;* orcid.org/0000-0002-5187-4555

Olga Nazarenko − *Laboratory of Inorganic Chemistry, Department of Chemistry and Applied Biosciences, ETH Zürich, 8093 Zürich, Switzerland; Laboratory for Thin Films and Photovoltaics, EMPA−Swiss Federal Laboratories for Materials Science and Technology, 8600 Dübendorf, Switzerland*

Nicola Colonna − *Laboratory for Neutron Scattering and Imaging, Paul Scherrer Institute, 5232 Villigen-PSI, Switzerland; National Centre for Computational Design and Discovery of Novel Materials (MARVEL), École Polytechnique Fédérale de Lausanne, 1015 Lausanne, Switzerland;* orcid.org/0000-0002-6106-6316

Nicola Marzari − *National Centre for Computational Design and Discovery of Novel Materials (MARVEL), École Polytechnique Fédérale de Lausanne, 1015 Lausanne, Switzerland;* orcid.org/0000-0002-9764-0199

Maksym V. Kovalenko − *Laboratory of Inorganic Chemistry, Department of Chemistry and Applied Biosciences, ETH Zürich, 8093 Zürich, Switzerland; Laboratory for Thin Films and Photovoltaics, EMPA−Swiss Federal Laboratories for Materials Science and Technology, 8600 Dübendorf, Switzerland*

Marco Grioni − *Institute of Physics and Lausanne Centre for Ultrafast Science (LACUS), École Polytechnique Fédérale de Lausanne, 1015 Lausanne, Switzerland*

Complete contact information is available at: https://pubs.acs.org/10.1021/acs.nanolett.1c03941

Notes

The authors declare no competing financial interest.

ACKNOWLEDGMENTS

This work was supported by the European Research Council via the Advanced Grants Horizon 2020 695197 DYNAMOX, by the Swiss National Science Foundation through the NCCR MUST and grant R'EQUIP 206021_182994, and by the Max Planck-EPFL Center for Molecular Nanoscience and Technology. The work at ETH Zurich (D.N.D. and M.V.K) was supported by the Swiss National Science Foundation (grant agreement 186406, in conjunction with SPP219 through DFG-SNSF bilateral program) and by the ETH Zurich through ETH + Project SynMatLab.

REFERENCES

(1) Chen, X.; Wang, Y.; Song, J.; Li, X.; Xu, J.; Zeng, H.; Sun, H. Temperature Dependent Reflectance and Ellipsometry Studies on a CsPbBr3 Single Crystal. *J. Phys. Chem. C* **2019**, *123*, 10564−10570.

(2) Tong, J.; et al. Carrier Lifetimes of > 1 μs in Sn-Pb Perovskites Enable Efficient All-Perovskite Tandem Solar Cells. *Science* **2019**, *364*, 475−479.

(3) Leijtens, T.; Bush, K. A.; Prasanna, R.; McGehee, M. D. Opportunities and Challenges for Tandem Solar Cells Using Metal Halide Perovskite Semiconductors. *Nat. Energy* **2018**, *3*, 828−838.

(4) Subbiah, A. S.; Isikgor, F. H.; Howells, C. T.; De Bastiani, M.; Liu, J.; Aydin, E.; Furlan, F.; Allen, T. G.; Xu, F.; Zhumagali, S.; Hoogland, S.; Sargent, E. H.; McCulloch, I.; De Wolf, S. High-Performance Perovskite Single-Junction and Textured Perovskite/Silicon Tandem Solar Cells via Slot-Die-Coating. *ACS Energy Lett.* **2020**, *5*, 3034−3040.

(5) Shang, Q.; Li, M.; Zhao, L.; Chen, D.; Zhang, S.; Chen, S.; Gao, P.; Shen, C.; Xing, J.; Xing, G.; Shen, B.; Liu, X.; Zhang, Q. Role of the Exciton−Polariton in a Continuous-Wave Optically Pumped CsPbBr3 Perovskite Laser. *Nano Lett.* **2020**, *20*, 6636−6643.

(6) Yakunin, S.; Protesescu, L.; Krieg, F.; Bodnarchuk, M. I.; Nedelcu, G.; Humer, M.; De Luca, G.; Fiebig, M.; Heiss, W.; Kovalenko, M. V. Low-Threshold Amplified Spontaneous Emission and Lasing from Colloidal Nanocrystals of Caesium Lead Halide Perovskites. *Nat. Commun.* **2015**, *6*, 8056.

(7) Zhang, Q.; Ha, S. T.; Liu, X.; Sum, T. C.; Xiong, Q. Room-Temperature Near-Infrared High-Q Perovskite Whispering-Gallery Planar Nanolasers. *Nano Lett.* **2014**, *14*, 5995−6001.

(8) Zhang, L.; Yang, X.; Jiang, Q.; Wang, P.; Yin, Z.; Zhang, X.; Tan, H.; Yang, Y. M.; Wei, M.; Sutherland, B. R.; Sargent, E. H.; You, J. Ultra-Bright and Highly Efficient Inorganic Based Perovskite Light-Emitting Diodes. *Nat. Commun.* **2017**, *8*, 15640.

(9) Schanze, K. S.; Kamat, P. V.; Yang, P.; Bisquert, J. Progress in Perovskite Photocatalysis. *ACS Energy Lett.* **2020**, *5*, 2602−2604.

(10) Huang, H.; Pradhan, B.; Hofkens, J.; Roeffaers, M. B. J.; Steele, J. A. Solar-Driven Metal Halide Perovskite Photocatalysis: Design, Stability, and Performance. *ACS Energy Lett.* **2020**, *5*, 1107−1123.

(11) Hickey, C. L.; Grumstrup, E. M. Direct Correlation of Charge Carrier Transport to Local Crystal Quality in Lead Halide Perovskites. *Nano Lett.* **2020**, *20*, 5050−5056.

(12) Sung, J.; Schnedermann, C.; Ni, L.; Sadhanala, A.; Chen, R. Y. S.; Cho, C.; Priest, L.; Lim, J. M.; Kim, H.-K.; Monserrat, B.; Kukura, P.; Rao, A. Long-Range Ballistic Propagation of Carriers in Methylammonium Lead Iodide Perovskite Thin Films. *Nat. Phys.* **2020**, *16*, 171−176.

(13) Kennedy, C. L.; Hill, A. H.; Grumstrup, E. M. Screening Links Transport and Recombination Mechanisms in Lead Halide Perovskites. *J. Phys. Chem. C* **2019**, *123*, 15827−15833.

(14) Delor, M.; Weaver, H. L.; Yu, Q.; Ginsberg, N. S. Imaging Material Functionality through Three-Dimensional Nanoscale Tracking of Energy Flow. *Nat. Mater.* **2020**, *19*, 56−62.

(15) Liu, W.; Yu, H.; Li, Y.; Hu, A.; Wang, J.; Lu, G.; Li, X.; Yang, H.; Dai, L.; Wang, S.; Gong, Q. Mapping Trap Dynamics in a CsPbBr3 Single-Crystal Microplate by Ultrafast Photoemission Electron Microscopy. *Nano Lett.* **2021**, *21*, 2932−2938.

(16) Niesner, D. Surface Electronic Structure and Dynamics of Lead Halide Perovskites. *APL Materials* **2020**, *8*, 090704.
(17) Puppin, M.; et al. Evidence of Large Polarons in Photoemission Band Mapping of the Perovskite Semiconductor $CsPbBr_3$. *Phys. Rev. Lett.* **2020**, *124*, 206402.
(18) Becker, M. A.; et al. Bright Triplet Excitons in Caesium Lead Halide Perovskites. *Nature* **2018**, *553*, 189−193.
(19) Stavrakas, C.; Delport, G.; Zhumekenov, A. A.; Anaya, M.; Chahbazian, R.; Bakr, O. M.; Barnard, E. S.; Stranks, S. D. Visualizing Buried Local Carrier Diffusion in Halide Perovskite Crystals via Two-Photon Microscopy. *ACS Energy Lett.* **2020**, *5*, 117−123.
(20) Béchu, S.; Ralaiarisoa, M.; Etcheberry, A.; Schulz, P. Photoemission Spectroscopy Characterization of Halide Perovskites. *Adv. Energy Mater.* **2020**, *10*, 1904007.
(21) Das, C.; Wussler, M.; Hellmann, T.; Mayer, T.; Zimmermann, I.; Maheu, C.; Nazeeruddin, M. K.; Jaegermann, W. Surface, Interface, and Bulk Electronic and Chemical Properties of Complete Perovskite Solar Cells: Tapered Cross-Section Photoelectron Spectroscopy, a Novel Solution. *ACS Appl. Mater. Interfaces* **2020**, *12*, 40949−40957.
(22) Powell, C. J. Practical Guide for Inelastic Mean Free Paths, Effective Attenuation Lengths, Mean Escape Depths, and Information Depths in x-Ray Photoelectron Spectroscopy. *Journal of Vacuum Science & Technology A* **2020**, *38*, 023209.
(23) Manser, J. S.; Christians, J. A.; Kamat, P. V. Intriguing Optoelectronic Properties of Metal Halide Perovskites. *Chem. Rev.* **2016**, *116*, 12956−13008.
(24) Kovalenko, M. V.; Protesescu, L.; Bodnarchuk, M. I. Properties and Potential Optoelectronic Applications of Lead Halide Perovskite Nanocrystals. *Science* **2017**, *358*, 745−750.
(25) Tao, S.; Schmidt, I.; Brocks, G.; Jiang, J.; Tranca, I.; Meerholz, K.; Olthof, S. Absolute Energy Level Positions in Tin- and Lead-Based Halide Perovskites. *Nat. Commun.* **2019**, *10*, 1−10.
(26) Yang, K.; Li, F.; Hu, H.; Guo, T.; Kim, T. W. Surface Engineering towards Highly Efficient Perovskite Light-Emitting Diodes. *Nano Energy* **2019**, *65*, 104029.
(27) Correa-Baena, J.-P.; Saliba, M.; Buonassisi, T.; Grätzel, M.; Abate, A.; Tress, W.; Hagfeldt, A. Promises and Challenges of Perovskite Solar Cells. *Science* **2017**, *358*, 739−744.
(28) Dirin, D. N.; Cherniukh, I.; Yakunin, S.; Shynkarenko, Y.; Kovalenko, M. V. Solution-Grown CsPbBr3 Perovskite Single Crystals for Photon Detection. *Chem. Mater.* **2016**, *28*, 8470−8474.
(29) Brittman, S.; Luo, J. A Promising Beginning for Perovskite Nanocrystals: A Nano Letters Virtual Issue. *Nano Lett.* **2018**, *18*, 2747−2750.
(30) Miyata, K.; Nagaoka, R.; Hada, M.; Tanaka, T.; Mishima, R.; Kuroda, T.; Sueta, S.; Iida, T.; Yamashita, Y.; Nishikawa, T.; Tsuruta, K.; Hayashi, Y.; Onda, K.; Kiwa, T.; Teranishi, T. Liquid-like Dielectric Response Is an Origin of Long Polaron Lifetime Exceeding 10 μs in Lead Bromide Perovskites. *J. Chem. Phys.* **2020**, *152*, 084704.
(31) Evans, T. J. S.; Miyata, K.; Joshi, P. P.; Maehrlein, S.; Liu, F.; Zhu, X.-Y. Competition Between Hot-Electron Cooling and Large Polaron Screening in CsPbBr3 Perovskite Single Crystals. *J. Phys. Chem. C* **2018**, *122*, 13724−13730.
(32) Munson, K. T.; Doucette, G. S.; Kennehan, E. R.; Swartzfager, J. R.; Asbury, J. B. Vibrational Probe of the Structural Origins of Slow Recombination in Halide Perovskites. *J. Phys. Chem. C* **2019**, *123*, 7061−7073.
(33) Miyata, K.; Meggiolaro, D.; Trinh, M. T.; Joshi, P. P.; Mosconi, E.; Jones, S. C.; Angelis, F. D.; Zhu, X.-Y. Large Polarons in Lead Halide Perovskites. *Science Advances* **2017**, *3*, No. e1701217.
(34) Kaur, G.; Ghosh, H. N. Hot Carrier Relaxation in CsPbBr3-Based Perovskites: A Polaron Perspective. *J. Phys. Chem. Lett.* **2020**, *11*, 8765−8776.
(35) Kang, J.; Wang, L.-W. High Defect Tolerance in Lead Halide Perovskite $CsPbBr_3$. *J. Phys. Chem. Lett.* **2017**, *8*, 489−493.
(36) Steirer, K. X.; Schulz, P.; Teeter, G.; Stevanovic, V.; Yang, M.; Zhu, K.; Berry, J. J. Defect Tolerance in Methylammonium Lead Triiodide Perovskite. *ACS Energy Lett.* **2016**, *1*, 360−366.
(37) Schilcher, M. J.; Robinson, P. J.; Abramovitch, D. J.; Tan, L. Z.; Rappe, A. M.; Reichman, D. R.; Egger, D. A. The Significance of Polarons and Dynamic Disorder in Halide Perovskites. *ACS Energy Lett.* **2021**, *6*, 2162−2173.
(38) Guzelturk, B.; et al. Visualization of Dynamic Polaronic Strain Fields in Hybrid Lead Halide Perovskites. *Nat. Mater.* **2021**, *20*, 618.
(39) Qiao, L.; Fang, W.-H.; Long, R.; Prezhdo, O. V. Photoinduced Dynamics of Charge Carriers in Metal Halide Perovskites from an Atomistic Perspective. *J. Phys. Chem. Lett.* **2020**, *11*, 7066−7082.
(40) Ziegler, J. D.; Zipfel, J.; Meisinger, B.; Menahem, M.; Zhu, X.; Taniguchi, T.; Watanabe, K.; Yaffe, O.; Egger, D. A.; Chernikov, A. Fast and Anomalous Exciton Diffusion in Two-Dimensional Hybrid Perovskites. *Nano Lett.* **2020**, *20*, 6674−6681.
(41) Duan, H.-G.; Tiwari, V.; Jha, A.; Berdiyorov, G. R.; Akimov, A.; Vendrell, O.; Nayak, P. K.; Snaith, H. J.; Thorwart, M.; Li, Z.; Madjet, M. E.; Miller, R. J. D. Photoinduced Vibrations Drive Ultrafast Structural Distortion in Lead Halide Perovskite. *J. Am. Chem. Soc.* **2020**, *142*, 16569−16578.
(42) Guo, Z.; Wan, Y.; Yang, M.; Snaider, J.; Zhu, K.; Huang, L. Long-Range Hot-Carrier Transport in Hybrid Perovskites Visualized by Ultrafast Microscopy. *Science* **2017**, *356*, 59−62.
(43) Sung, J.; Macpherson, S.; Rao, A. Enhanced Ballistic Transport of Charge Carriers in Alloyed and K-Passivated Alloyed Perovskite Thin Films. *J. Phys. Chem. Lett.* **2020**, *11*, 5402−5406.
(44) Wang, Z.; Lin, Q.; Wenger, B.; Christoforo, M. G.; Lin, Y.-H.; Klug, M. T.; Johnston, M. B.; Herz, L. M.; Snaith, H. J. High Irradiance Performance of Metal Halide Perovskites for Concentrator Photovoltaics. *Nature Energy* **2018**, *3*, 855−861.
(45) Zhu, H.; Trinh, M. T.; Wang, J.; Fu, Y.; Joshi, P. P.; Miyata, K.; Jin, S.; Zhu, X.-Y. Organic Cations Might Not Be Essential to the Remarkable Properties of Band Edge Carriers in Lead Halide Perovskites. *Adv. Mater.* **2017**, *29*, 1603072.
(46) Kulbak, M.; Gupta, S.; Kedem, N.; Levine, I.; Bendikov, T.; Hodes, G.; Cahen, D. Cesium Enhances Long-Term Stability of Lead Bromide Perovskite-Based Solar Cells. *J. Phys. Chem. Lett.* **2016**, *7*, 167−172.
(47) Zhang, C.; Fernando, J. F. S.; Firestein, K. L.; von Treifeldt, J. E.; Siriwardena, D.; Fang, X.; Golberg, D. Thermal Stability of CsPbBr3 Perovskite as Revealed by in Situ Transmission Electron Microscopy. *APL Materials* **2019**, *7*, 071110.
(48) Chan, C. C. S.; Fan, K.; Wang, H.; Huang, Z.; Novko, D.; Yan, K.; Xu, J.; Choy, W. C. H.; Lončarić, I.; Wong, K. S. Uncovering the Electron-Phonon Interplay and Dynamical Energy-Dissipation Mechanisms of Hot Carriers in Hybrid Lead Halide Perovskites. *Adv. Energy Mater.* **2021**, *11*, 2003071.
(49) Li, M.; Fu, J.; Xu, Q.; Sum, T. C. Slow Hot-Carrier Cooling in Halide Perovskites: Prospects for Hot-Carrier Solar Cells. *Adv. Mater.* **2019**, *31*, 1802486.
(50) Palmieri, T.; Baldini, E.; Steinhoff, A.; Akrap, A.; Kollár, M.; Horváth, E.; Forró, L.; Jahnke, F.; Chergui, M. Mahan Excitons in Room-Temperature Methylammonium Lead Bromide Perovskites. *Nat. Commun.* **2020**, *11*, 850.
(51) Nie, Z.; Gao, X.; Ren, Y.; Xia, S.; Wang, Y.; Shi, Y.; Zhao, J.; Wang, Y. Harnessing Hot Phonon Bottleneck in Metal Halide Perovskite Nanocrystals via Interfacial Electron−Phonon Coupling. *Nano Lett.* **2020**, *20*, 4610−4617.
(52) Yang, J.; et al. Acoustic-Optical Phonon up-Conversion and Hot-Phonon Bottleneck in Lead-Halide Perovskites. *Nat. Commun.* **2017**, *8*, 1−9.
(53) Sekiguchi, F.; Hirori, H.; Yumoto, G.; Shimazaki, A.; Nakamura, T.; Wakamiya, A.; Kanemitsu, Y. Enhancing the Hot-Phonon Bottleneck Effect in a Metal Halide Perovskite by Terahertz Phonon Excitation. *Phys. Rev. Lett.* **2021**, *126*, 077401.
(54) Frost, J. M.; Whalley, L. D.; Walsh, A. Slow Cooling of Hot Polarons in Halide Perovskite Solar Cells. *ACS Energy Lett.* **2017**, *2*, 2647−2652.
(55) Manser, J. S.; Kamat, P. V. Band Filling with Free Charge Carriers in Organometal Halide Perovskites. *Nat. Photonics* **2014**, *8*, 737−743.

https://doi.org/10.1021/acs.nanolett.1c03941
Nano Lett. 2022, 22, 1067−1074

(56) Fu, J.; Xu, Q.; Han, G.; Wu, B.; Huan, C. H. A.; Leek, M. L.; Sum, T. C. Hot Carrier Cooling Mechanisms in Halide Perovskites. *Nat. Commun.* **2017**, *8*, 1−9.
(57) Li, Q.; Yang, Y.; Que, W.; Lian, T. Size- and Morphology-Dependent Auger Recombination in CsPbBr3 Perovskite Two-Dimensional Nanoplatelets and One-Dimensional Nanorods. *Nano Lett.* **2019**, *19*, 5620−5627.
(58) Kang, Y.; Han, S. Intrinsic Carrier Mobility of Cesium Lead Halide Perovskites. *Phys. Rev. Applied* **2018**, *10*, 044013.
(59) Wais, M.; Eckstein, M.; Fischer, R.; Werner, P.; Battiato, M.; Held, K. Quantum Boltzmann Equation for Strongly Correlated Systems: Comparison to Dynamical Mean Field Theory. *Phys. Rev. B* **2018**, *98*, 134312.
(60) Nguyen, X. T.; Timmer, D.; Rakita, Y.; Cahen, D.; Steinhoff, A.; Jahnke, F.; Lienau, C.; De Sio, A. Ultrafast Charge Carrier Relaxation in Inorganic Halide Perovskite Single Crystals Probed by Two-Dimensional Electronic Spectroscopy. *J. Phys. Chem. Lett.* **2019**, *10*, 5414−5421.
(61) Poncé, S.; Schlipf, M.; Giustino, F. Origin of Low Carrier Mobilities in Halide Perovskites. *ACS Energy Lett.* **2019**, *4*, 456−463.
(62) Gehrmann, C.; Egger, D. A. Dynamic Shortening of Disorder Potentials in Anharmonic Halide Perovskites. *Nat. Commun.* **2019**, *10*, 3141.
(63) Bagsican, F. R. G.; Wais, M.; Komatsu, N.; Gao, W.; Weber, L. W.; Serita, K.; Murakami, H.; Held, K.; Hegmann, F. A.; Tonouchi, M.; Kono, J.; Kawayama, I.; Battiato, M. Terahertz Excitonics in Carbon Nanotubes: Exciton Autoionization and Multiplication. *Nano Lett.* **2020**, *20*, 3098−3105.
(64) Sajedi, M.; Krivenkov, M.; Marchenko, D.; Varykhalov, A.; Sánchez-Barriga, J.; Rienks, E. D. L.; Rader, O. Absence of a Giant Rashba Effect in the Valence Band of Lead Halide Perovskites. *Phys. Rev. B* **2020**, *102*, 081116.
(65) Saidaminov, M. I.; Haque, M. A.; Almutlaq, J.; Sarmah, S.; Miao, X.-H.; Begum, R.; Zhumekenov, A. A.; Dursun, I.; Cho, N.; Murali, B.; Mohammed, O. F.; Wu, T.; Bakr, O. M. Inorganic Lead Halide Perovskite Single Crystals: Phase-Selective Low-Temperature Growth, Carrier Transport Properties, and Self-Powered Photodetection. *Advanced Optical Materials* **2017**, *5*, 1600704.
(66) Rakita, Y.; Kedem, N.; Gupta, S.; Sadhanala, A.; Kalchenko, V.; Böhm, M. L.; Kulbak, M.; Friend, R. H.; Cahen, D.; Hodes, G. Low-Temperature Solution-Grown CsPbBr3 Single Crystals and Their Characterization. *Cryst. Growth Des.* **2016**, *16*, 5717−5725.
(67) Endres, J.; Egger, D. A.; Kulbak, M.; Kerner, R. A.; Zhao, L.; Silver, S. H.; Hodes, G.; Rand, B. P.; Cahen, D.; Kronik, L.; Kahn, A. Valence and Conduction Band Densities of States of Metal Halide Perovskites: A Combined Experimental−Theoretical Study. *J. Phys. Chem. Lett.* **2016**, *7*, 2722−2729.
(68) Ghaithan, H. M.; Alahmed, Z. A.; Qaid, S. M. H.; Hezam, M.; Aldwayyan, A. S. Density Functional Study of Cubic, Tetragonal, and Orthorhombic CsPbBr3 Perovskite. *ACS Omega* **2020**, *5*, 7468−7480.
(69) Chen, Z.; Lee, M.-i.; Zhang, Z.; Diab, H.; Garrot, D.; Lédée, F.; Fertey, P.; Papalazarou, E.; Marsi, M.; Ponseca, C.; Deleporte, E.; Tejeda, A.; Perfetti, L. Time-Resolved Photoemission Spectroscopy of Electronic Cooling and Localization in CH3NH3PbI3 Crystals. *Phys. Rev. Materials* **2017**, *1*, 045402.
(70) Haight, R. Electron Dynamics at Surfaces. *Surf. Sci. Rep.* **1995**, *21*, 275−325.
(71) Scajev, P.; Litvinas, D.; Soriute, V.; Kreiza, G.; Stanionyte, S.; Jursenas, S. Crystal Structure Ideality Impact on Bimolecular, Auger, and Diffusion Coefficients in Mixed-Cation CsxMA1−xPbBr3 and CsxFA1−xPbBr3 Perovskites. *J. Phys. Chem. C* **2019**, *123*, 23838−23844.
(72) Scajev, P.; Aleksiejunas, R.; Miasojedovas, S.; Nargelas, S.; Inoue, M.; Qin, C.; Matsushima, T.; Adachi, C.; Jursenas, S. Two Regimes of Carrier Diffusion in Vapor-Deposited Lead-Halide Perovskites. *J. Phys. Chem. C* **2017**, *121*, 21600−21609.
(73) Sridharan, A.; Noel, N. K.; Rand, B. P.; Kéna-Cohen, S. Role of Photon Recycling and Band Filling in Halide Perovskite Photoluminescence under Focussed Excitation Conditions. *J. Phys. Chem. C* **2021**, *125*, 2240−2249.
(74) Arias, D. H.; Moore, D. T.; van de Lagemaat, J.; Johnson, J. C. Direct Measurements of Carrier Transport in Polycrystalline Methylammonium Lead Iodide Perovskite Films with Transient Grating Spectroscopy. *J. Phys. Chem. Lett.* **2018**, *9*, 5710−5717.
(75) Ryu, H.; Byun, H. R.; McCall, K. M.; Park, D. Y.; Kim, T. J.; Jeong, M. S.; Kanatzidis, M. G.; Jang, J. I. Role of the A-Site Cation in Low-Temperature Optical Behaviors of APbBr3 (A = Cs, CH3NH3). *J. Am. Chem. Soc.* **2021**, *143*, 2340−2347.
(76) Makarov, N. S.; Guo, S.; Isaienko, O.; Liu, W.; Robel, I.; Klimov, V. I. Spectral and Dynamical Properties of Single Excitons, Biexcitons, and Trions in Cesium−Lead-Halide Perovskite Quantum Dots. *Nano Lett.* **2016**, *16*, 2349−2362.
(77) Oguri, K.; Tsunoi, T.; Kato, K.; Nakano, H.; Nishikawa, T.; Tateno, K.; Sogawa, T.; Gotoh, H. Dynamical Observation of Photo-Dember Effect on Semi-Insulating GaAs Using Femtosecond Core-Level Photoelectron Spectroscopy. *Appl. Phys. Express* **2015**, *8*, 022401.
(78) Svirskas, S.; Balciunas, S.; Simenas, M.; Usevicius, G.; Kinka, M.; Velicka, M.; Kubicki, D.; Castillo, M. E.; Karabanov, A.; Shvartsman, V. V.; de Rosario Soares, M.; Sablinskas, V.; Salak, A. N.; Lupascu, D. C.; Banys, J. Phase Transitions, Screening and Dielectric Response of CsPbBr3. *J. Mater. Chem. A* **2020**, *8*, 14015−14022.
(79) Yang, Z.; Surrente, A.; Galkowski, K.; Miyata, A.; Portugall, O.; Sutton, R. J.; Haghighirad, A. A.; Snaith, H. J.; Maude, D. K.; Plochocka, P.; Nicholas, R. J. Impact of the Halide Cage on the Electronic Properties of Fully Inorganic Cesium Lead Halide Perovskites. *ACS Energy Lett.* **2017**, *2*, 1621−1627.
(80) Haug, A. Carrier Density Dependence of Auger Recombination. *Solid-State Electron.* **1978**, *21*, 1281−1284.
(81) Shen, J.-X.; Zhang, X.; Das, S.; Kioupakis, E.; de Walle, C. G. V. Unexpectedly Strong Auger Recombination in Halide Perovskites. *Adv. Energy Mater.* **2018**, *8*, 1801027.
(82) Kioupakis, E.; Yan, Q.; Steiauf, D.; de Walle, C. G. V. Temperature and Carrier-Density Dependence of Auger and Radiative Recombination in Nitride Optoelectronic Devices. *New J. Phys.* **2013**, *15*, 125006.
(83) Lundstrom, M.; Jeong, C. *Near-Equilibrium Transport: Fundamentals and Applications*; World Scientific: 2013; pp 33−57.
(84) Hill, A. H.; Kennedy, C. L.; Massaro, E. S.; Grumstrup, E. M. Perovskite Carrier Transport: Disentangling the Impacts of Effective Mass and Scattering Time Through Microscopic Optical Detection. *J. Phys. Chem. Lett.* **2018**, *9*, 2808−2813.
(85) Zhu, H.; Miyata, K.; Fu, Y.; Wang, J.; Joshi, P. P.; Niesner, D.; Williams, K. W.; Jin, S.; Zhu, X.-Y. Screening in Crystalline Liquids Protects Energetic Carriers in Hybrid Perovskites. *Science* **2016**, *353*, 1409−1413.
(86) Lv, B.; Qian, T.; Ding, H. Angle-Resolved Photoemission Spectroscopy and Its Application to Topological Materials. *Nat. Rev. Phys.* **2019**, *1*, 609−626.

https://doi.org/10.1021/acs.nanolett.1c03941
Nano Lett. 2022, 22, 1067−1074